BJ Biomolecules

Biochem. J. (2013) **456**, 397–407 (Printed in Great Britain) doi:10.1042/BJ20131003

online data

Solution structures of the *Bacillus cereus* metallo-β-lactamase BcII and its complex with the broad spectrum inhibitor *R*-thiomandelic acid

Andreas Ioannis KARSISIOTIS*†, Christian F. DAMBLON*‡ and Gordon C. K. ROBERTS*[1]

*The Henry Wellcome Laboratories of Structural Biology, Department of Biochemistry, University of Leicester, Leicester LE1 9HN, U.K., †The School of Pharmacy and Pharmaceutical Sciences, Biomedical Sciences Research Institute, University of Ulster, Coleraine BT52 1SA, Northern Ireland, U.K., and ‡Chimie Biologique Structurale, Institut de Chimie, Université de Liège, 4000 Liège, Belgium

Metallo-β-lactamases, enzymes which inactivate β-lactam antibiotics, are of increasing biological and clinical significance as a source of antibiotic resistance in pathogenic bacteria. In the present study we describe the high-resolution solution NMR structures of the *Bacillus cereus* metallo-β-lactamase BcII and of its complex with *R*-thiomandelic acid, a broad-spectrum inhibitor of metallo-β-lactamases. This is the first reported solution structure of any metallo-β-lactamase. There are differences between the solution structure of the free enzyme and previously reported crystal structures in the loops flanking the active site, which are important for substrate and inhibitor binding and catalysis. The binding of *R*-thiomandelic acid and the roles of active-site residues are defined in detail. Changes in the enzyme structure upon inhibitor binding clarify the role of the mobile β3–β4 loop. Comparisons with other metallo-β-lactamases highlight the roles of individual amino-acid residues in the active site and the β3–β4 loop in inhibitor binding and provide information on the basis of structure–activity relationships among metallo-β-lactamase inhibitors.

Key words: antibiotic resistance, enzyme structure, inhibitor binding, metallo-β-lactamase, NMR spectroscopy, zinc enzyme.

INTRODUCTION

The rapid increase in resistance to β-lactam antibiotics is a major clinical and public health concern, as these antibiotics have long been key to the treatment of serious bacterial infections. The β-lactamases, enzymes which inactivate β-lactam antibiotics by hydrolysis of their endocyclic β-lactam bond, are a major source of this resistance [1]. In the sequence-based Ambler classification of β-lactamases, classes A, C and D are serine enzymes, whereas class B represents the zinc-dependent MBLs (metallo-β-lactamases) [2,3]; the latter are of particular concern since they are located on highly transmissible plasmids and have a broad spectrum of activity against almost all β-lactam antibiotics. MBLs are grouped according to sequence similarities and zinc co-ordination into three subclasses, B1, B2 and B3 [2,4,5]. Subclasses B1 and B3, operating with one or two zinc atoms, are broad-spectrum enzymes acting on almost all β-lactam substrates apart from monobactams, whereas subclass B2 enzymes, operating with one zinc atom, are strict carbapenemases acting poorly on penicillins and cephalosporins. MBLs in all three subclasses give rise to clinical problems [6,7]. The VIM and IMP families of transferable subclass B1 MBLs have a worldwide spread and are encountered in several Gram-negative pathogenic bacteria. In addition, the occurrence of new transferable MBLs such as NDM-1 [8] is an indicator of a serious, evolving and escalating problem.

A number of X-ray crystal structures of MBLs have been determined, a list of which can be found on the MBLED (Metallo-Beta-Lactamase Engineering Database; http://www.mbled.uni-stuttgart.de/) [5], mostly of enzymes of the ubiquitous and clinically relevant B1 subclass such as BcII, CcrA, IMP-1, BlaB, SPM-1, VIM-2 and NDM-1, but also including structures of members of the B2 and B3 subclasses. All known MBL structures share the same topology, an $\alpha\beta/\beta\alpha$ sandwich fold; this so-called MBL fold defines a rapidly expanding family of zinc metallo-hydrolases [10].

By contrast with the success in developing inhibitors of serine β-lactamases such as clavulanic acid, no clinically efficient inhibitors of MBLs have yet been reported [11,12]. Whereas all MBLs share conserved motifs, the sequence similarity is low and the range of active site architectures makes the development of broad spectrum inhibitors difficult. Crystal structures have been determined for complexes of MBLs with several different inhibitors [13–20], but although the *Bacillus cereus* MBL BcII is the most extensively studied MBL, no structure for an inhibitor complex of this enzyme has hitherto been reported.

It is clear that the most promising inhibitors directly co-ordinate one or both zinc atoms through, for example, thiol [21], carboxylate [17], tetrazole [13] or hydrazone [22] groups, and thiol-containing compounds show activity as broad-spectrum MBL inhibitors [20,21,23]. The potency of the thiol plus carboxylate combination is well established; even the simplest mercaptocarboxylate compounds, such as mercaptoacetic acid and 2-mercaptopropionic acid, are potent inhibitors of subclass B1 MBLs ([24–26] and S. Kumar, A.I. Karsisiotis, C. F. Damblon and G.C.K. Roberts, unpublished work). We have previously identified *R*-thiomandelate as a promising reasonably broad-spectrum inhibitor of MBLs, combining a thiol functionality which binds simultaneously to the two zinc atoms with a carboxylate function which increases its inhibitory potency

Abbreviations used: HSQC, heteronuclear single-quantum coherence; MBL, metallo-β-lactamase; NOE, nuclear Overhauser effect.

[1] To whom correspondence should be addressed (email gcr@le.ac.uk).

The complete ^{1}H, ^{13}C and ^{15}N chemical shifts and NMR restraints have been deposited in the BioMagResBank (BMRB) under accession codes 19047 (BcII) and 19048 (BcII–*R*-thiomandelic acid) and co-ordinates have been deposited in the PDB under accession codes 2M5C (BcII) and 2M5D (BcII–*R*-thiomandelic acid).

[21,27]. We now report the solution structures of *B. cereus* BcII, a representative member of the important subclass B1 of the MBL family, alone and in its complex with *R*-thiomandelate. Analysis of the structures throws new light on the function of the much-discussed 'mobile loop' or 'flap' (the $\beta3$–$\beta4$ loop), which is conserved in B1 MBLs and plays a role in inhibitor binding and catalytic activity [3,14,16,17,28–30], and on the enzyme–ligand interactions which are likely to be important for inhibitor design.

EXPERIMENTAL

Protein production and purification

Singly (^{15}N) and doubly (^{13}C, ^{15}N) labelled samples of BcII and the BcII–thiomandelate complex were produced as described previously [31].

NMR spectroscopy and sequence-specific assignments

All NMR experiments were performed at 308 K in 20 mM Mes, pH 6.4, containing 10 % $^{2}H_2O$, 100 mM NaCl and 0.2 mM $ZnCl_2$. Backbone and side chain sequence-specific assignments were obtained using standard triple resonance and TOCSY experiments as described prevously [31]. NOEs (nuclear Overhauser effects) were assigned in ^{15}N-edited [32,33] and ^{13}C-edited [34] NOESY-HSQC (heteronuclear single-quantum coherence) spectra, acquired at 600 MHz (cryoprobe) and 800 MHz (cryoprobe) respectively, with a mixing time of 80 ms. A ^{13}C-edited NOESY-HSQC [34] spectrum at 800 MHz, optimized for the aromatic region, was used for obtaining both side chain assignments of the aromatic residues and NOE constraints.

^{13}C-filtered experiments [35] (with ^{13}C-protein and natural abundance ligand) provided unambiguous assignments of the resonances of the CαH (benzylic proton; 5.223 p.p.m.) and the *ortho* aromatic protons (6.941 p.p.m.) of the bound thiomandelate. Both shifts were verified by a series of double-filtered experiments. The observation that the two *ortho* protons are magnetically equivalent indicates that the aromatic ring of bound thiomandelate can 'flip' rapidly by 180°, as is commonly observed for phenylalanine and tyrosine residues in proteins [36] and for aromatic rings of bound ligands (e.g. [37]). The chemical shifts of the *meta*- and *para*- protons of the aromatic ring of the inhibitor appeared to be degenerate.

Structural calculations and automated NOE assignments

Automated NOE assignments and structure calculations were performed using the CANDID module [38] and the torsion angle dynamics algorithm CYANA 2.1 [39] using default calibration parameters and optimized chemical shift tolerance windows. All NOESY peaks were picked using the peak-picking mode in Sparky (http://www.cgl.ucsf.edu/home/sparky) for individual strips with noise and artefact peaks removed manually. Peak lists in the DYANA/XEASY format were prepared using Sparky. The finalized peak lists used for the structural calculations before refinement were produced through several rounds of manual peak checks and automated unbiased NOE assignment runs using the CANDID module, aiming for optimum cycle1 and final CYANA target function values, maximum assignment percentages and numbers of generated constraints and improved structural parameters. This iterative process produced better constraint sets and, through the manual inspection of the NOESY spectrum, resolved missing or incomplete assignments. Ligand–protein distance constraints were obtained from experiments, using ^{13}C-protein and natural abundance ligand, designed to detect NOEs between protons bound to ^{13}C and protons not bound to ^{13}C. Out of the 13 NOE-derived constraints obtained, four were assigned to the CαH of *R*-thiomandelate. The remaining nine constraints were assigned to one of the pseudoatoms (QG for the *ortho* protons, QD for the *meta* protons and QR for all the ring protons) of the thiomandelate ring on the basis of criteria including chemical shifts, probable distance in preliminary structural calculations and relative intensities of the corresponding peaks. Cross-peak heights were used for NOE distance calibration. Hydrogen bond restraints within secondary-structure elements were identified by the first no-violations refinement run. Only those observed in over 75 % of the calculated structures were considered and were cross-validated with deuterium exchange experiments prior to introduction into the refinement. Automated stereospecific assignments from CYANA were introduced at the start of refinement. As discussed in the Supplementary Online Data and Table S1 (at http://www.biochemj.org/bj/456/bj4560397add.htm), the structures were calculated both with and without dihedral angle constraints obtained from the TALOS [41] database and we focus on the structures obtained without dihedral constraints; Table 1 gives the structural statistics for the structures calculated without TALOS constraints and Supplementary Table S2 (at http://www.biochemj.org/bj/456/bj4560397add.htm) gives these statistics for structures calculated with these constraints. The structures calculated with and without dihedral angle constraints had very similar RMSD values (0.35–0.38 for backbone atoms) and similar Ramachandran statistics (>98 % of residues in the core and allowed regions), but the structures calculated with dihedral angle constraints showed significantly more distance and angle violations.

Structure refinement and validation

CYANA/CANDID distance constraints were used directly in structure refinement since the final calculation filters out ambiguous distance constraints. The two metal atoms and, in the case of the complex, the inhibitor molecule, were incorporated through the use of the generic linker system present in CYANA as described in the Supplementary Online Data. The refinement protocol used consisted of five cycles of simulated annealing with a high start temperature (8000 K) and a gradual slow cooling to a low temperature (100 K) in a large number of steps (20000). This standard torsion angle-based simulating annealing protocol with all constraints applied simultaneously is combined with cycles of redundant dihedral angle constraints (REDAC; [42]). Several cycles of this combined refinement protocol, which eliminates violations and progressively reduces target function values while improving local and overall quality, were used to generate the final converged structures. Out of an ensemble of 100 converged structures generated, the 20 best (lowest CYANA target function during refinement) structures were selected. Structure validation was carried out using PROCHECK-NMR [43], WHAT-IF [44] and the iCING (https://lamp-lbi-43.rcs.le.ac.uk/icing/#welcome) web interface. All molecular models were viewed and assessed using MOLMOL [45], which was used for all RMSD calculations and comparisons (typically from the bundle of the 20 lowest energy structures). All distance restraint distribution plots are based on the CYANA macro 'dcostat'.

Databank accession codes

The complete ^{1}H, ^{13}C and ^{15}N chemical shifts and NMR restraints have been deposited in the BMRB (BioMagResBank) under

Table 1 Structural statistics and agreement with experimental data for the refined structures of BcII and the BcII–*R*-thiomandelate complex

Target function, RMSD and energy values are calculated for a bundle of 20 structures unless specified otherwise. RTM, *R*-thiomandelate.

Parameter	Statistics	Free BcII	Complex
CYANA / CANDID	Input NOE peaks	13088	12499
	Unassigned peaks	1071	1131
	Assignment percentage	91.8	91.0
	Target function (cycle1)	247.9	204.92
	Target function (final)	7.03	3.71
RMSD, Å (residues 7–227) cycle1	Backbone/heavy atoms	1.07/1.53	1.32/1.75
RMSD, Å (residues 7–227) final	Backbone/heavy atoms	0.30/0.67	0.36/0.72
NOE constraints	Upper distance limits	7190	6578
	Short range ($i=1$)	3001	2797
	Medium range ($1<i\leqslant4$)	1277	1059
	Long range ($i>4$)	2912	2722
	Removed during refinement	9	2
Other constraints	Zinc distance constraints	7	9
	RTM constraints	-	13
	Dihedral restraints*	0	0
	Hydrogen bonds	42	36
	Stereospecific assignments	143	109
Target function (refinement)	Minimum	3.34	2.22
	Average (20 structures)	4.3 ± 0.4	2.4 ± 0.1
	Average (50 structures)	4.9 ± 0.6	2.6 ± 0.2
RMSD of experimental restraints (20 structures)	Upper distance limits (Å)	0.007 ± 0.001	0.004 ± 0.0002
	Lower distance limits (Å)	0.002 ± 0.002	0.002 ± 0.001
	Torsion angles (°)	0.01 ± 0.01	0.008 ± 0.016
Van der Waals energy sums	20 structures	19 ± 1	11.1 ± 0.6
	50 structures	21 ± 2	12 ± 1
Mean violations (20/50 structures)	Distance >0.5 Å	0/0	$0/0.02\pm0.14$
	Angle >5°	$0/0.2\pm0.6$	0/0
	Van der Waals	0/0	0/0
RMSD, Å (residues 7–227) final structures	Backbone/heavy atoms	0.35/0.72	0.38/0.73
Ramachandran statistics (CANDID stage/refinement)	Core (%)	71.3/70.4	70.6/70.8
	Allowed (%)	27.2/27.9	28.6/27.6
	Generously allowed (%)	1.0/1.0	0.3/0.8
	Disallowed (%)	0.5/0.6	0.5/0.8

*The structures were calculated with no external (TALOS) dihedral angle input. (The statistics for structures calculated with inclusion of the dihedral angle constraints are given in Supplementary Table S2 at http://www.biochemj.org/bj/456/bj4560397add.htm.)

accession codes 19047 (BcII) and 19048 (BcII–*R*-thiomandelic acid) and co-ordinates have been deposited in the PDB under accession codes 2M5C (BcII) and 2M5D (BcII–*R*-thiomandelic acid).

RESULTS AND DISCUSSION

Resonance assignments and structure calculations

The strategy for obtaining the sequence-specific assignments has been described previously [31]. ^{1}H, ^{13}C and ^{15}N resonances were assigned to over 96 % completion for both free BcII and the BcII–inhibitor complex. Automated NOE assignments and structure calculations were performed using the CANDID/CYANA protocol as described in the Experimental section. The CANDID stage of the calculations yielded 91.8 % and 91.0 % assignment of all NOE peaks for the free enzyme and complex respectively. The solution structures were calculated using 7190 (∼31 per residue) non-ambiguous NOE distance restraints for the free enzyme and 6578 (∼29 per residue) for the complex with *R*-thiomandelate. All structures were refined to the point where there were no angle violations larger than 5° and no distance violations larger than 0.2 Å (1 Å = 0.1 nm) in 80 % of the structures. The key statistics for the structure calculations are presented in Table 1.

The solution structure of the free enzyme: comparison with crystal structures

The structure of BcII shown in Figures 1(A) and 1(B) is the first solution structure reported for any MBL. As indicated by the RMSD values given in Table 1, the structure is well defined by the NMR data. The overall fold clearly corresponds to the classic MBL fold, of the four-layered $\alpha\beta/\beta\alpha$ class, with a central β-sheet sandwich flanked on either side by α-helices; the active site, with the two zinc ions, is at one edge of the β-sheet sandwich, flanked by two long loops [residues 33–38(60–66) and 170–188(223–241)]. {All residue numbers are presented as: number in BcII sequence(number in standard BBL system) [4].} The RMSD values between the member of the NMR structure ensemble closest to the mean and the 1BVT crystal structure [46], chosen for comparison since it has the highest resolution of the crystal structures reported for BcII, are 1.25 Å for the backbone and 1.96 Å for all heavy atoms, when comparing the parts of the protein which are well-defined in the NMR structure (residues 8–226). If the $\beta3$–$\beta4$ loop and residues 11–15 (see below) are excluded from the comparison, the backbone RMSD between the two structures drops to 1.00 Å. The zinc co-ordination geometry is also very similar in solution and in the crystal (Supplementary Figure S1 at http://www.biochemj.org/bj/456/bj4560397add.htm), although it should be noted that the two highest-resolution crystal structures were obtained at significantly lower pH (pH 5.2–5.6 [46,47]) than

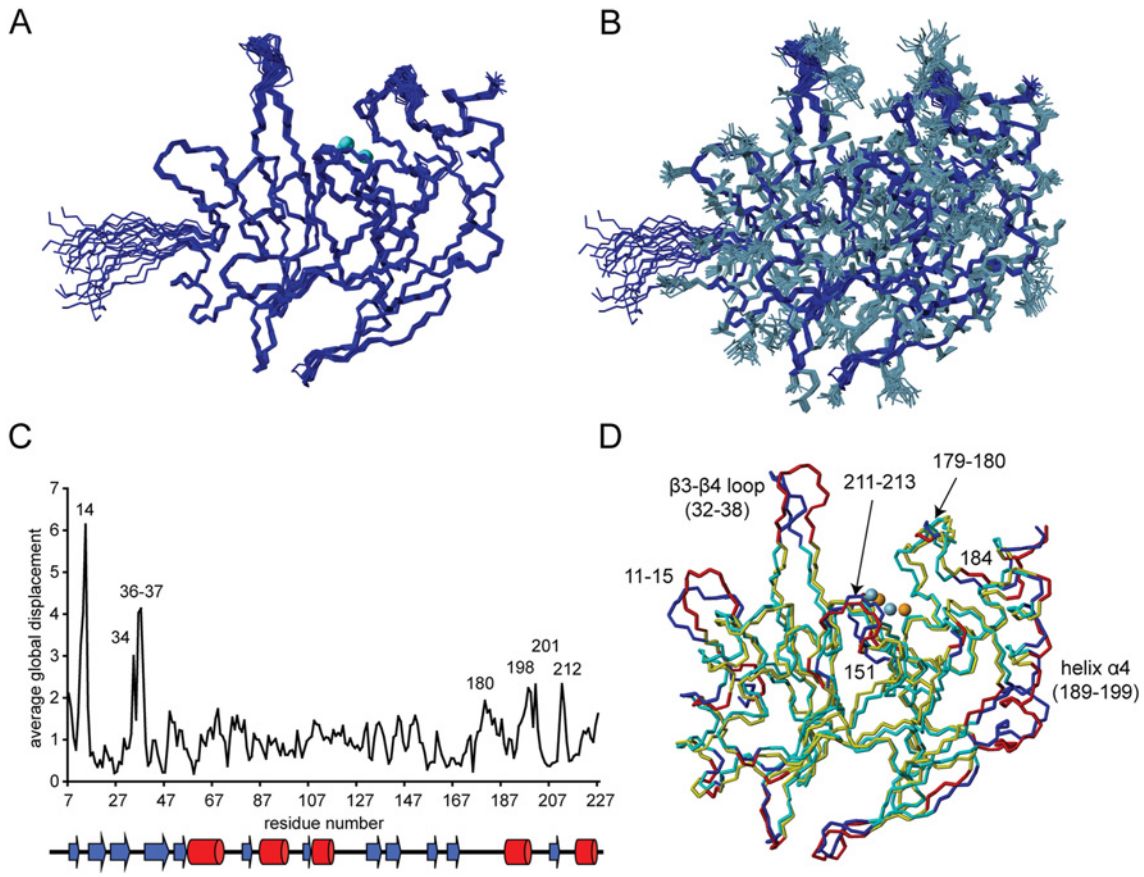

Figure 1 Solution structure of MBL BcII

A bundle of 20 structures are shown with (**A**) only the protein backbone depicted in blue (zinc atoms in cyan) and (**B**) the amino acid side chains (heavy atoms, residues 7–227) also included in grey. (**C**) Average global displacement values comparing the BcII crystal structure (PDB code 1BVT) and the free enzyme solution structure as a function of the amino acid sequence with secondary structure elements indicated. (**D**) Comparison of the crystal structure (PDB code 1BVT) in yellow and the solution structure in cyan, the regions with RMSD>0.4 Å being highlighted in red and blue respectively. The solution structure shown is the member of the ensemble of 20 lowest energy structures closest to the mean structure (calculated with MOLMOL).

the solution structure (pH 6.4) and the nature of the anions in solution is different.

As can be seen in Figures 1(C) and 1(D), the secondary structure elements of the structure are closely similar in solution and the crystal, the regions with RMSD >0.4 Å being largely restricted to surface loops. Three of these are worthy of comment: (i) residues 11–15(36–40); (ii) the β3–β4 loop [residues 33–38(60–66)]; and (iii) the β11–α4 loop and helix α4 [residues 170–199(223–252)]. The construct used in the crystallographic study [46] was six residues shorter at the N-terminus than that used in the present study. Perhaps, as a result, residues 11–14 appear to be flexible in the 1BVT structure and were modelled with zero occupancy in the crystal, explaining the observed differences from the solution structure.

The active site of BcII is flanked by two loops, β3–β4 [residues 32–38(60–66)] and β11–α4 [residues 170–188(223–241)]. The main variability between the different crystal structures of BcII is encountered in the β3–β4 loop, the 'mobile loop' or 'flap', where all crystal structures show very poor or missing electron density. Many of the residues of this loop are either missing from the PDB files (1BC2, 2BC2, 3BC2 and 1BMC) or, in the case of 1BVT, where residues 32–38 are displayed with zero occupancy, are modelled according to other MBL structures. In the solution structure, although this surface loop has, as would be expected, a higher RMSD within the NMR structural ensemble than residues in the structural core of the protein (Figure 1), it does have a relatively well-defined conformation. This conformation is consistently seen in all the calculated NMR structures and, importantly, it is well supported by a substantial NOE network covering even residues at the tip of the loop (Supplementary Figure S2 at http://www.biochemj.org/bj/456/bj4560397add.htm); a similar well-defined NOE network has been reported for the corresponding loop of CcrA MBL, although a structure was not calculated [48]. The structure in the present study thus represents the first reliable depiction of the conformation of this functionally important loop in the uncomplexed BcII enzyme. Importantly, the conformation is significantly different from that modelled in 1BVT, displaying a twist (Figure 1 and Supplementary Figure S2) which brings the side chains of some of the loop residues (notably Phe[34] and Val[39]) into a more central position over the active-site cavity.

The conformation of the long β11–α4 loop [residues 170–188(223–241)] on the opposite side of the active-site cleft shows modest differences between solution and crystal structure, mostly in the backbone of the highly conserved residues Gly[179] and Asn[180]. Perhaps, as a result, there is a small displacement [0.7 Å on average for residues 189–199(242–252)] of the penultimate

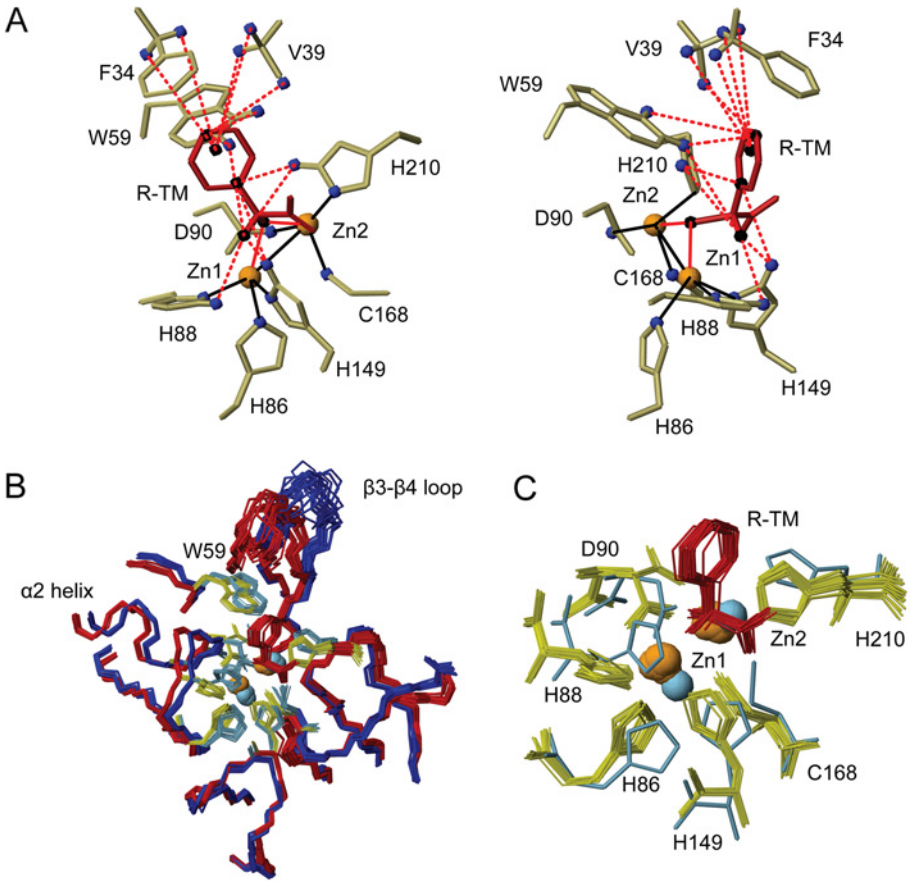

Figure 2 The active site of the BcII–thiomandelate complex

(**A**) Two views of the lowest energy structure illustrating the constraints based on NOEs detected between the enzyme and thiomandelate. These constraints are depicted as red broken lines and the atoms and pseudoatoms involved in these constraints are shown as blue or black spheres. The inhibitor is shown in red and the zinc atoms are depicted as orange spheres. The zinc-co-ordination constraints are represented by black lines and constraints between the zinc atoms and the inhibitor sulfur atom are represented by red solid lines. (**B**) Superimposition (on residues with RMSD $<$0.45 Å) of the solution NMR structures (bundle of 20 lowest energy structures) of BcII (blue, side chains light blue) and the BcII–thiomandelate complex (red, side chains yellow, inhibitor red), focusing on the important active site residues. (**C**) Detail of the BcII–thiomandelate complex structure highlighting the metal co-ordinating residues and the zinc atoms (a single free enzyme structure is included as reference in light blue). (**B**) and (**C**) have the same orientation.

helix (α4) of BcII in solution as compared with the crystal structure.

The structure of the BcII–thiomandelate complex

Information on enzyme–inhibitor contacts in the complex was obtained from detection of NOEs between protons of the enzyme and the bound inhibitor, using ^{13}C-filtered NOESY experiments. The network of 13 inhibitor–enzyme NOE constraints is shown in Figure 2(A). NOEs are detected between the benzylic (Hα) proton of the inhibitor and the imidazole HE1 protons of His$^{88(118)}$, His$^{149(196)}$ and His$^{210(263)}$ as well as the HH2 proton of the indole ring of Trp$^{59(87)}$. Additionally, the *ortho* protons of the aromatic ring of the inhibitor show NOE connectivities with the HE1 protons of His$^{149(196)}$ and His$^{210(263)}$, and the *meta* protons with the indole HH2 and HZ2 protons of Trp$^{59(87)}$. There are also ambiguous NOEs (assigned to the QR pseudoatom for the whole thiomandelate ring) to both methyl and C$_\beta$ protons of Val$^{39(67)}$ and the C$_\beta$ protons of Phe$^{34(61)}$. In addition we used two constraints connecting the sulfur atom of thiomandelate to each of the two zinc atoms; we demonstrated previously [27] that the thiolate group of thiomandelate co-ordinates to the two metal ions in cadmium-substituted BcII.

The overall structure of the enzyme–inhibitor complex (Figure 3A) is well-defined by the NMR data (RMSD for heavy atoms of 0.73 Å over residues 7–227) and is very similar to that of the free enzyme (Figure 3B). The local backbone RMSD profile (Figure 3C) of the BcII–thiomandelate complex is also similar to that of the free enzyme, with high values in the expected regions, such as the β3–β4 and the β11–α4 loops and the unstructured N-terminus (see also Supplementary Figure S3 at http://www.biochemj.org/bj/456/bj4560397add.htm). Detailed structural comparisons will focus on the active site and on the two loops which flank it.

The BcII–thiomandelate complex: the active-site cavity and the zinc ligands

The protein–ligand NOEs shown in Figure 2(A) define the location of the inhibitor in the active-site cavity quite precisely (Figures 2B and 2C). Comparing the free enzyme and the inhibitor complex by superimposing those parts of the two structures which have RMSD $<$0.45 Å, it appears that the polypeptide segment 85–91(115–121) at the end of the β6–α2 loop opens up slightly on inhibitor binding, increasing the space in the active-site cavity. Large chemical shift perturbations are observed for these

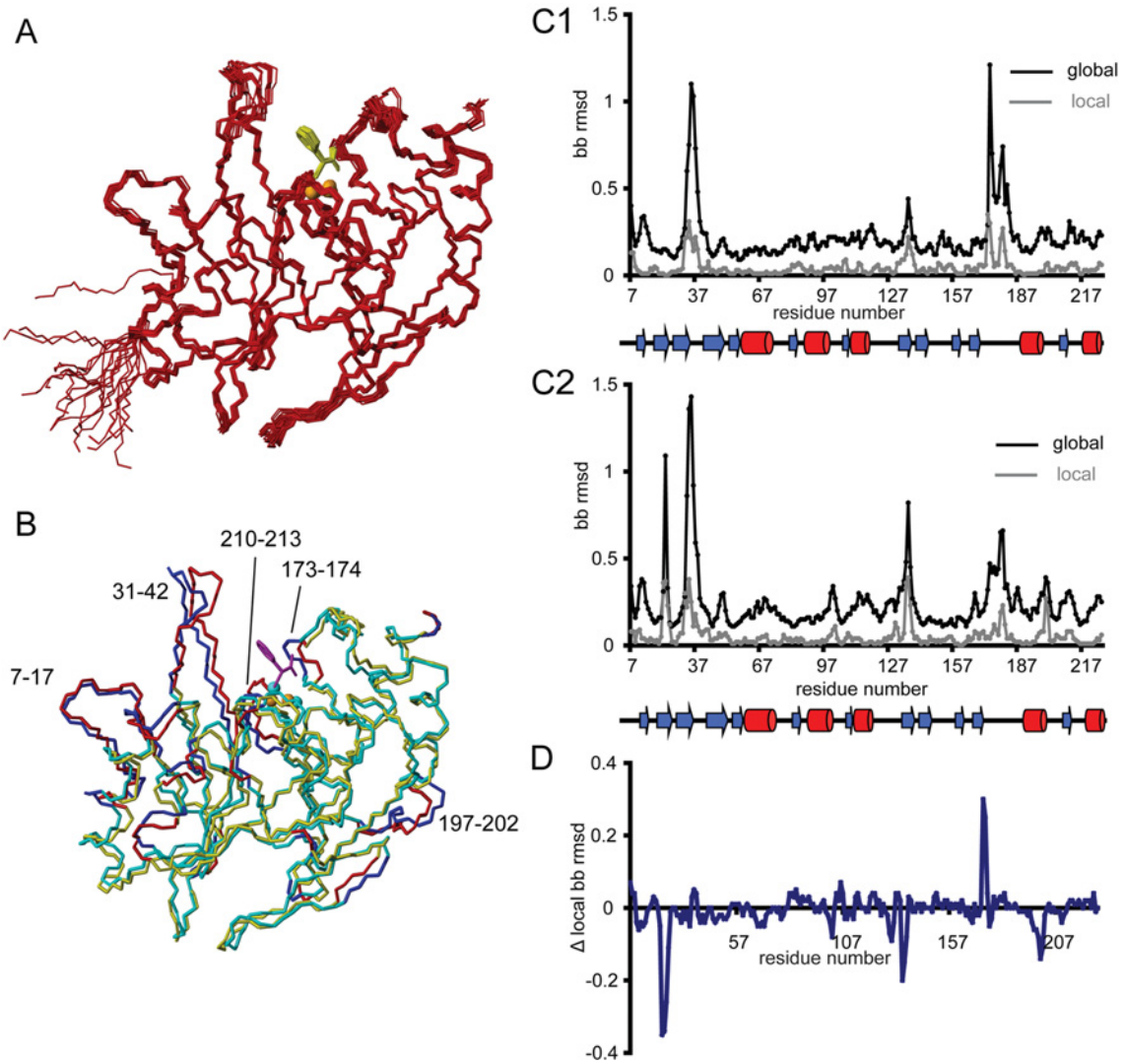

Figure 3 Solution structure of the BcII–thiomandelate complex

(**A**) A bundle of 20 low-energy structures is shown; the protein backbone is coloured red, the zinc atoms are depicted as orange spheres and the inhibitor molecule is coloured yellow. (**B**) Comparison of the solution structures of the free enzyme (in cyan) and the complex (in yellow) with the regions with RMSD >0.45 Å highlighted in blue and red respectively. The inhibitor molecule is coloured magenta. The structures are the lowest energy structures which are additionally the closest to the mean structures. (**C**) Average global (black) and local (grey) backbone RMSDs for the BcII solution structure (**C1**) and the BcII–thiomandelate complex solution structure (**C2**). (**D**) Difference between the local backbone RMSD values in the two structures. The RMSD values are shown as a function of the amino acid sequence with the secondary structure elements indicated.

residues (Figure 4), including the zinc ligands $His^{86(116)}$, $His^{88(118)}$ and $Asp^{90(120)}$; the effects on $Asp^{90(120)}$ are particularly large ($\Delta\delta$ $^{15}N = -5.071$, $H_N = +0.410$, $^{13}C_\alpha = -0.449$, $H_\alpha = +0.520$, $^{13}C_\beta = -1.184$, $H_{\beta 2} = +0.669$ and $H_{\beta 3} = -0.107$ p.p.m.). This movement of residues 85–91(115–121) is associated with a displacement of helix $\alpha 2$ [residues 92–101(122–131)] along its axis by approximately 1.3 Å (Figure 2B) and with changes in the side chain conformation of the three metal ligands, $His^{88(118)}$ having a clearly different conformation (Figure 2C). This latter residue is in close proximity to the bound inhibitor, showing an NOE from its HE1 proton to the CαH of thiomandelate.

The comparison of the structures of the free enzyme and the complex shown in Figures 2(B), 2(C) and 3(B) also suggests that the position of the zinc atoms changes significantly on thiomandelate binding. Some caution must be exercised in this comparison, since constraints on zinc–ligand and zinc–zinc distances were used to locate the metal ions in the structures (see the Supplementary Online Data). However, these constraints were identical in the determination of structures of the free enzyme and the complex and were only applied during structure refinement. The NOE-based constraint set, without metal co-ordination constraints, led to well-defined positions of the zinc ligands, closely similar to those after refinement (Supplementary Figure S4 at http://www.biochemj.org/bj/456/bj4560397add.htm). This gives one confidence that the differences in zinc position shown in Figure 2 can be attributed to the changes in the NOE constraint networks of the residues involved and are likely to be real. Recent high-resolution crystallographic and molecular dynamic studies of the B1 subclass MBL NDM-1 [49] emphasize that the zinc ions have the flexibility to move significantly within the active site. The changes in position of the zinc atoms on thiomandelate binding are likely to be the result of the facts that: (i) the bound inhibitor occupies space previously occupied by zinc ligands (notably His^{88} and Asp^{90}, Figure 2C), leading to changes in the position of these

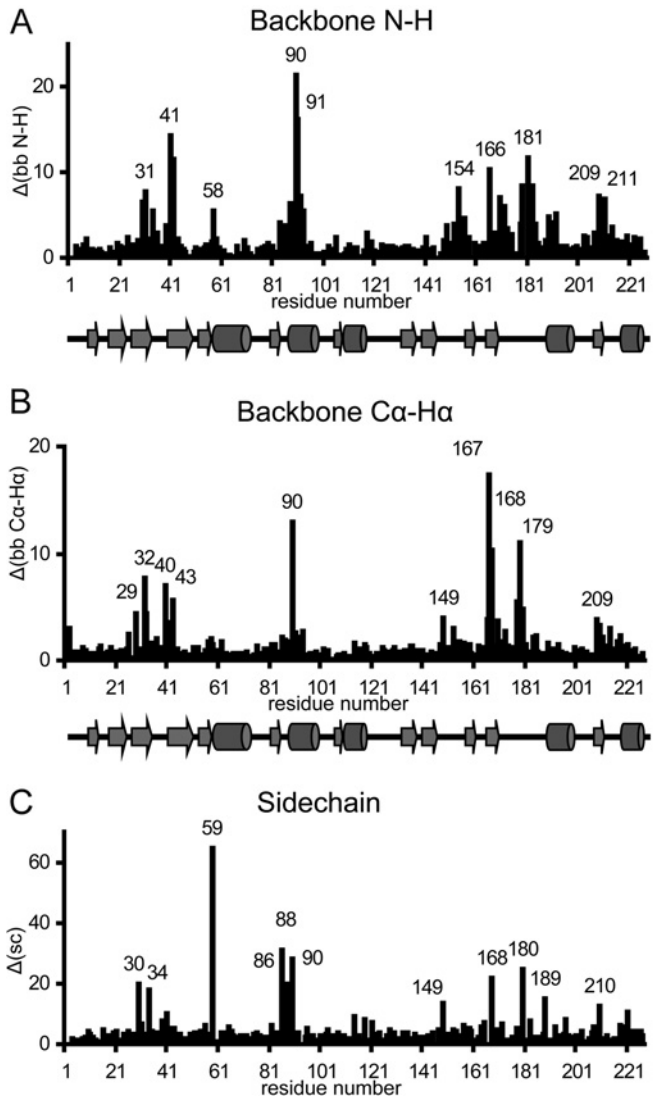

Figure 4 Chemical shift perturbations upon *R*-thiomandelate binding

Chemical shift differences are shown as a function of the amino acid sequence, with the secondary structure elements indicated. (**A**) Backbone N-H $[\sqrt{(\Delta H_\alpha/0.03)^2 + (\Delta N/0.3)^2}]$, (**B**) backbone C_α-H_α $[\sqrt{(\Delta H_\alpha/0.03)^2 + (\Delta C_\alpha/0.12)^2}]$, (**C**) side chain $[\sqrt{(\Delta H/0.03)^2 + (\Delta N/0.3)^2 + (\Delta C/0.12)^2}]$.

ligands; and (ii) the inhibitor sulfur which co-ordinates the metals in the complex has a larger radius than the oxygen of the water or hydroxide ion which co-ordinates them in the free enzyme.

The BcII–thiomandelate complex: the β11–α4 loop

The long β11–α4 loop [168–185(221–238)], which begins with the zinc ligand Cys$^{168(221)}$, contains some of the residues whose chemical shifts are most affected by thiomandelate binding (Figure 4). However, there is little structural change in this region of the enzyme and perturbations of side chain chemical shifts are generally larger than those of the backbone. The largest structural differences are seen for residues 173–176(226–228) and 179–180(232–233), the backbone of the loop moving somewhat further from the active-site cavity in the complex, again contributing to increasing the available space, although the differences in position between the two structures are small ($\leqslant$1.2 Å). There is evidence for a decrease in flexibility of this loop in the complex (Figure 3D), notably at residues Thr$^{173(226)}$ and Ser$^{174(227)}$; in the free enzyme the bundle of structures is divided into two subgroups of different backbone conformation for residues 173–174 creating the high local RMSD values. The backbone amide ^{1}H and ^{15}N resonances of Asn$^{180(233)}$ are not observed in the spectrum of the free enzyme, but become observable in that of the complex, again suggesting some decreased mobility on inhibitor binding.

In the crystal structures of the IMP-1 and VIM-2 MBLs with mercaptocarboxylate inhibitors [16,50], residues in this loop interact with the carboxylate group of the inhibitor; an asparagine residue equivalent to Asn$^{180(233)}$ in BcII is seen to interact with the carboxylate in both structures, and a lysine residue equivalent to Lys$^{171(224)}$ in BcII interacts in the IMP-1 complex (in the VIM-2 enzyme the equivalent residue is a tyrosine). In our earlier docking of thiomandelate into the crystal structure of free BcII [27], we assumed that Lys^{171} did indeed interact with the inhibitor carboxylate group. However, the structure of the complex we have now determined shows clearly that, even though the Lys^{171} side chain faces the carboxylate of the inhibitor, the distances between the two oxygen atoms and the NZ atom of Lys^{171} are too great (5.27 and 4.97 Å) to allow a direct interaction. Similarly, the side chain of Asn^{180} is relatively near the inhibitor carboxylate (6.3 Å for HB3 and 7.7 Å for HD21), but too distant for a direct interaction. The positions of these two side chains are well supported by an NOE network involving surrounding residues (see Supplementary Figure S5 at http://www.biochemj.org/bj/456/bj4560397add.htm). Importantly, the covalent structures of the mercaptocarboxylate inhibitors studied by Concha et al. [16] and Yamaguchi et al. [50] are such that the carboxylate is further from the zinc-co-ordinating thiolate group than is the case for thiomandelate. Assuming that the primary interaction is that between the inhibitor thiolate and the zinc atoms, this difference in inhibitor structure presumably accounts for the inability of the carboxylate of thiomandelate to interact directly with Lys^{171} and Asn^{180}, although it is entirely possible that an interaction mediated by a bound water molecule may be present in the case of Lys^{171}.

The BcII–thiomandelate complex: the β3–β4 mobile loop and the hydrophobic pocket

The β3–β4 mobile loop or flap [residues 32–39(59–67)] of B1 MBLs has been shown to play a role in substrate and inhibitor binding, and catalysis [30]. With the exception of a glycine residue at position 63 (BBL numbering), none of the residues in the loop is fully conserved, although the residues corresponding to Phe$^{34(61)}$ and Val$^{39(67)}$ are hydrophobic in all B1 class MBLs. The IMP-1 and CcrA MBLs have a loop which is one residue longer, and have a tryptophan residue near the tip of the loop at position 64 (BBL numbering) which interacts with the bound ligand [14,16,17,28], but makes only a modest contribution to the binding energy of thiomandelate and another mercaptocarboxylate inhibitor [30]. In these enzymes there is a significant decrease in mobility of the loop upon inhibitor binding [48,51] and it moves towards the bound inhibitor [16]. In the BcII–thiomandelate complex, the aromatic ring of the inhibitor interacts with residues Phe$^{34(61)}$ and Val$^{39(67)}$ in the loop as well as with Trp$^{59(87)}$ which is situated at the base of the loop; these residues form a conserved hydrophobic pocket which is clearly important for binding the inhibitor (Figure 2A). Chemical shifts of all the residues in the β3–β4 loop are perturbed to some degree (Figure 4). The effects, especially on backbone chemical shifts, are greatest for residues at the base of the loop, and in addition residues in the β5–α1 loop [residues 56–60(84–88)], at the base of the β3–β4 loop, are clearly affected.

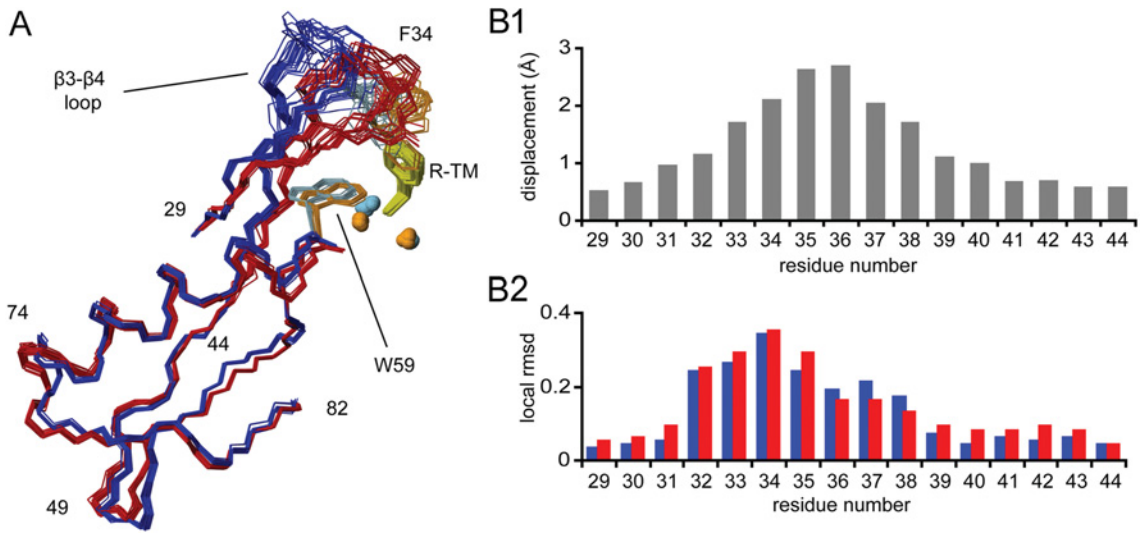

Figure 5 Structure and variability of the $\beta3$–$\beta4$ loop

(**A**) Amino acids 29–82, encompassing the $\beta3$–$\beta4$ loop, are highlighted in the superimposition of the free enzyme (blue) and complex (red) structures. The side chains of Trp^{59} and Phe^{34} are light blue (free enzyme) or orange (complex). The inhibitor molecule is yellow and the zinc atoms are cyan (free enzyme) or orange (complex). (**B**) Backbone global displacement values (**B1**) highlighting the movement of the $\beta3$–$\beta4$ loop, and local backbone RMSDs for the two structures (**B2**; free enzyme blue and complex red) for residues 29–44 as a function of residue number.

Indeed, $Trp^{59(87)}$ is the most affected of all residues in terms of chemical shifts, with three protons of the indole ring showing upfield shifts of as much as 0.678 p.p.m., reflecting its proximity to the aromatic ring of thiomandelate in an edge-to-face orientation. [In IMP-1 and CcrA, $Trp^{59(87)}$, otherwise conserved in B1 MBLs, is replaced by a phenylalanine residue which also contributes to the hydrophobic pocket involved in inhibitor binding.]

Thiomandelate, a relatively small molecule, makes less extensive interactions with residues in the $\beta3$–$\beta4$ loop compared with many of the other inhibitors whose binding to MBLs has been studied crystallographically. However, these interactions do lead to a substantial movement (up to 2.5 Å) of the loop towards the inhibitor (Figure 5A). This movement is somewhat less than that seen in the complex of IMP-1 with a much larger mercaptocarboxylate inhibitor, where Val^{25} and Val^{29} are displaced by approximately 2.9 Å [16]. It is likely that in MBLs with a tryptophan residue at the tip of the loop (CcrA, IMP family) the interactions of this residue with the inhibitor lead to a rather greater movement of the loop than in those enzymes where this tryptophan is absent (BcII, VIM family).

As discussed above, in the free enzyme the $\beta3$–$\beta4$ loop has a quite well-defined conformation, notwithstanding the relatively large RMSD values which would be expected for a surface loop. The same is true of the BcII–inhibitor complex, where the conformation of this loop is again well-defined by an extensive network of NOEs (Supplementary Figure S2). Comparing the structures of the free enzyme and the complex in this region (Figure 5A) suggests that there is a hinge-like motion of the loop on inhibitor binding, reflected in the fact that the displacement is at a maximum at the tip of the loop (Figure 5B1), with its local conformation being largely unaffected. This motion does not appear to be accompanied by any decrease in flexibility; the local backbone RMSD of the loop residues does not change significantly upon inhibitor binding (Figure 5B2). This is in contrast with a number of crystallographic studies where, as discussed above, electron density for the $\beta3$–$\beta4$ loop is often missing in the free enzyme, but the conformation of this loop becomes well-defined in complexes with inhibitors. The fact that a significant degree of flexibility in this loop is retained in the complex, notwithstanding its direct interactions with the inhibitor, would of course still be compatible with the maintenance of a hydrophobic pocket for the aromatic ring of thiomandelate.

Structure–activity relationships for inhibitor binding to B1 and B3 MBLs

In attempting to design improved inhibitors of MBLs which might be of clinical value, there are two distinct issues: improving affinity and retaining a broad spectrum of activity against MBLs of all classes. Thiomandelate is a potent ($K_i = 30$–500 nM) inhibitor of subclass B1 and B3 MBLs, which are di-zinc enzymes, but is a much poorer inhibitor ($K_i = 144$ μM) of the subclass B2 CphA enzyme from *Aeromonas hydrophila* [21]. The CphA enzyme functions as a mono-zinc enzyme, and is a strict carbapenemase [2]; we have shown that mercaptocarboxylate inhibitors bind quite differently to this enzyme, with the carboxylate interacting with the zinc atoms [20].

In the present study we will focus on the implications of the elucidated structures for the design of high-affinity inhibitors of subclass B1 (including the clinically important IMP, VIM and NDM enzymes) and B3 MBLs. It is clear that the interaction of the thiolate group with the zinc ions is the major determinant of the affinity of mercaptocarboxylate inhibitors for the B1 and B3 enzymes [21]. The importance of the thiolate–zinc interaction will restrict the possibility of substitutions on the inhibitor close to the thiolate; the structure of the BcII–thiomandelate complex clearly shows that the benzylic carbon (Cα) of the inhibitor is close to the zinc ligands $His^{88(118)}$ and $His^{149(196)}$ and substitution at this position would be unfavourable.

As we have noted previously [20], two regions of the active-site cavity which could be exploited in inhibitor design are a conserved hydrophobic pocket and a conserved hydrogen-bonding region, shown in Figure 6. The latter comprises residues in the $\beta11$–$\alpha4$ loop [see above; residues 170–188(223–241)]. This loop is shown in brown in Figure 6, with $Lys^{171(224)}$, $Asn^{180(233)}$ and $Asp^{183(236)}$ conserved as hydrogen-bonding residues in B1 enzymes shown in blue; in the B3 enzymes AIM-1 and SMB-1, residue

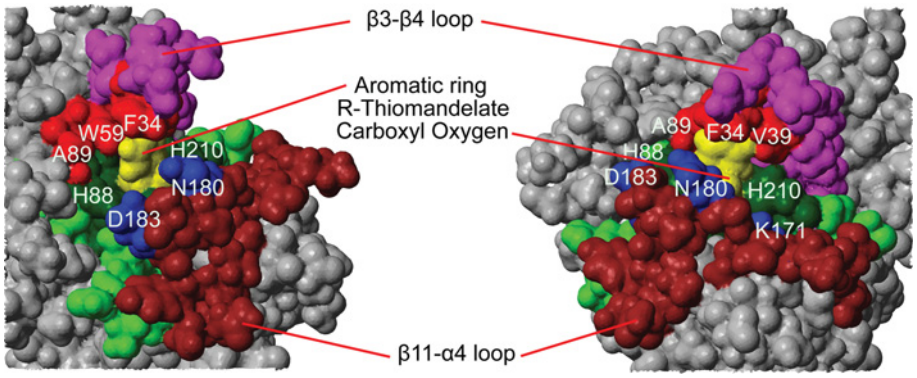

Figure 6 The active site of the BcII–thiomandelate complex

Two views of a van der Waals surface representation of the structure of the complex are shown. The bound *R*-thiomandelic acid is coloured yellow and the interacting or potentially interacting elements of BcII are coloured as follows: the β3–β4 loop (residues 29–43) is magenta, the metal co-ordinating residues are dark green [with adjacent residues in the sequence ($\pm$2 residues) shown in green] and the β11–α4 loop (residues 171–188) is brown. Residues forming a hydrophobic pocket are coloured red and conserved residues involved in potential hydrogen-bonding contacts are coloured blue. The rest of the protein is coloured grey. The zinc atoms are buried and invisible in this representation.

Gln^{157}, in an α4–β7(156–166) loop which is unique to the B3 subclass, is positioned similarly to Asn$^{180(233)}$ [26,52]. In B3 enzymes the loop corresponding to β11–α4 in BcII also includes serine, threonine, asparagine or tyrosine residues at positions 221, 223, 225 and 228 (BBL numbering), which may be involved in β-lactam recognition (see [26]) and thus can be targeted in inhibitor design. The carboxylate group of thiomandelate increases the affinity of the inhibitor for BcII ~100-fold [21], even though the structure shows that it is too far away for a direct interaction with Lys$^{171(224)}$ or Asn$^{180(233)}$. It is apparent from this and from the very potent inhibition of MBLs observed for some other mercaptocarboxylates [19,20,25,53–57] that the distance from thiolate to carboxylate is a key feature of the structure–activity relationship among these compounds. From the structure described in the present study, one or more methylene groups would need to be inserted between the benzylic carbon and the carboxylate group to allow the latter to interact with the conserved Lys$^{171(224)}$ and/or with Asn$^{180(233)}$ and a flexible linkage of this kind would also permit favourable interactions with the other hydrogen-bonding residues in this region in B3 enzymes.

Bulky hydrophobic groups, such as the aromatic ring of thiomandelate, forming contacts with non-polar residues on the mobile β3–β4 loop and/or hydrophobic pockets at the base of the loop, are encountered in the majority of B1 subclass MBL–inhibitor complexes whose structure has been determined [15–17,28] and are a common feature of an effective inhibitor. In Figure 6, residues of the β3–β4 loop are shown in magenta, with residues forming a hydrophobic pocket around the aromatic ring of the inhibitor shown in red. The flexibility of both the β3–β4 and the β11–α4 loops (notably the existence of an 'adaptable' hydrophobic pocket) undoubtedly contributes to the ability of MBLs to bind a structurally diverse range of inhibitors [30,58]. However, in the B3 enzyme the β3–β4 loop is much shorter, due to shorter β3 and β4 strands, and further away from the active site. In its place, it is the α3–β7 (in L1) or α4–β7 (in SMB-1) loop [26,59] which forms an equivalent lining to one side of the active site and contains hydrophobic residues which can interact with inhibitors [60]. The part of the aromatic ring of thiomandelate most accessible for substitution appears to be the *ortho* and *meta* positions, blocked by Phe$^{34(61)}$ and Val$^{39(67)}$ in the loop on one side but accessible on the other. In addition to the hydrophobic pocket formed by the β3–β4 loop in the B1 enzymes or the α3–β7/α4–β7 loop in the B3 enzymes, a number of residues in the β11–α4 loop [168–185(221–238)] with conserved hydrogen-bonding character are also suitably placed for interaction with such substituents. It is clear that, in view of the significant structural differences between B1 and B3 enzymes, for both the hydrogen-bonding region and the hydrophobic pocket, flexible substituents would be favoured for broad-spectrum activity.

Conclusions

The structure of BcII described in the present study is the first structure of a MBL in solution. Since the distribution of NMR constraints over the sequence has no significant gaps, we can conclude that this structure is a reliable representation of the structure in solution. By contrast, in the X-ray crystallographic structures electron density was missing for some important regions, such as the β3–β4 loop, and these were modelled with zero occupancy. The conformation of the β3–β4 loop observed in the solution structure of the free enzyme is the best available representation of this key region, which is involved in substrate and inhibitor binding. This loop has significant flexibility, but overall has a well-defined conformation. Comparison with the structure of the BcII–thiomandelate complex shows that this conformation is largely maintained, but the loop undergoes a hinge-like motion bringing key hydrophobic residues into contact with the bound inhibitor. The formation of a flexible hydrophobic pocket explains the ability of MBLs to bind substrates of a wide variety of structures. The key interaction of thiomandelate with the enzyme involves co-ordination of the thiolate group of the inhibitor with the two zinc atoms. The structure of the BcII–thiomandelate complex provides valuable information on the interactions which determine the structure–activity relationships among MBL inhibitors which will be useful in guiding the development of these compounds to help counteract the threat of widespread resistance to β-lactam antibiotics.

AUTHOR CONTRIBUTION

Andreas Ioannis Karsisiotis, Christian Damblon and Gordon Roberts designed the experiments. Andreas Ioannis Karsisiotis carried out the experimental work and, with Gordon Roberts, analysed the data. Andreas Ioannis Karsisiotis and Gordon Roberts wrote the paper.

ACKNOWLEDGEMENTS

We thank Dr Igor Barsukov and Dr Ben Goult for useful discussions and advice, Professor Chris Schofield for providing *R*-thiomandelate, Dr Eiso Ab for help and advice with the CYANA linker system and non-standard residues, Dr Fred Muskett for providing a refinement script combining simulated annealing and REDAC, and the National Institute for Medical Research NMR facilities at Mill Hill for the acquisition of a ^{13}C-edited NOESY-HSQC spectrum.

FUNDING

This work was supported by a European Research Training Network [contract HPRN-CT-2002-00264] and by the Biotechnology and Biological Sciences Research Council [grant number BBS/B/058855].

REFERENCES

1 Frère, J. M., Dubus, A., Galleni, M., Matagne, A. and Amicosante, G. (1999) Mechanistic diversity of β-lactamases. Biochem. Soc. Trans. **27**, 58–63
2 Bebrone, C. (2007) Metallo-β-lactamases (classification, activity, genetic organization, structure, zinc coordination) and their superfamily. Biochem. Pharmacol. **74**, 1686–1701
3 Palzkill, T. (2013) Metallo-β-lactamase structure and function. Ann. N.Y. Acad. Sci. **1277**, 91–104
4 Galleni, M., Lamotte-Brasseur, J., Rossolini, G. M., Spencer, J., Dideberg, O., Frère, J. M. and Metallo-β-Lactamase Working Group (2001) Standard numbering scheme for class B β-lactamases. Antimicrob. Agents Chemother. **45**, 660–663
5 Widmann, M., Pleiss, J. and Oelschlaeger, P. (2012) Systematic analysis of metallo-β-lactamases using an automated database. Antimicrob. Agents Chemother. **56**, 3481–3491
6 Fritsche, T. R., Sader, H. S., Toleman, M. A., Walsh, T. R. and Jones, R. N. (2005) Emerging metallo-β-lactamase-mediated resistances: a summary report from the worldwide SENTRY antimicrobial surveillance program. Clin. Infect. Dis. **41**, S276–S278
7 Cornaglia, G., Giamarellou, H. and Rossolini, G. M. (2011) Metallo-β-lactamases: a last frontier for β-lactams? Lancet Infect. Dis. **11**, 381–393
8 Nordmann, P., Poirel, L., Walsh, T. R. and Livermore, D. M. (2011) The emerging NDM carbapenemases. Trends Microbiol. **19**, 588–595
9 Reference deleted
10 Daiyasu, H., Osaka, K., Ishino, Y. and Toh, H. (2001) Expansion of the zinc metallo-hydrolase family of the β-lactamase fold. FEBS Lett. **503**, 1–6
11 Drawz, S. M. and Bonomo, R. A. (2010) Three decades of β-lactamase inhibitors. Clin. Microbiol. Rev. **23**, 160–201
12 Toney, J. H. and Moloughney, J. G. (2004) Metallo-β-lactamase inhibitors: promise for the future? Curr. Opin. Invest. Drugs **5**, 823–826
13 Toney, J. H., Cleary, K. A., Hammond, G. G., Yuan, X. L., May, W. J., Hutchins, S. M., Ashton, W. T. and Vanderwall, D. E. (1999) Structure-activity relationships of biphenyl tetrazoles as metallo-β-lactamase inhibitors. Bioorg. Med. Chem. Lett. **9**, 2741–2746
14 Payne, D. J., Hueso-Rodriguez, J. A., Boyd, H., Concha, N. O., Janson, C. A., Gilpin, M., Bateson, J. H., Cheever, C., Niconovich, N. L., Pearson, S. et al. (2002) Identification of a series of tricyclic natural products as potent broad-spectrum inhibitors of metallo-β-lactamases. Antimicrob. Agents Chemother. **46**, 1880–1886
15 Fitzgerald, P. M. D., Wu, J. K. and Toney, J. H. (1998) Unanticipated inhibition of the metallo-β-lactamase from *Bacteroides fragilis* by 4-morpholineethanesulfonic acid (MES): a crystallographic study at 1.85-Å resolution. Biochemistry **37**, 6791–6800
16 Concha, N. O., Janson, C. A., Rowling, P., Pearson, S., Cheever, C. A., Clarke, B. P., Lewis, C., Galleni, M., Frère, J. M., Payne, D. J. et al. (2000) Crystal structure of the IMP-1 metallo β-lactamase from *Pseudomonas aeruginosa* and its complex with a mercaptocarboxylate inhibitor: binding determinants of a potent, broad-spectrum inhibitor. Biochemistry **39**, 4288–4298
17 Toney, J. H., Hammond, G. G., Fitzgerald, P. M. D., Sharma, N., Balkovec, J. M., Rouen, G. P., Olson, S. H., Hammond, M. L., Greenlee, M. L. and Gao, Y. D. (2001) Succinic acids as potent inhibitors of plasmid-borne IMP-1 metallo-β-lactamase. J. Biol. Chem. **276**, 31913–31918
18 Kurosaki, H., Yamaguchi, Y., Yasuzawa, H., Jin, W. C., Yamagata, Y. and Arakawa, Y. (2006) Probing, inhibition, and crystallographic characterization of metallo-β-lactamase (IMP-1) with fluorescent agents containing dansyl and thiol groups. ChemMedChem **1**, 969–972
19 Garcia-Saez, I., Hopkins, J., Papamicael, C., Franceschini, N., Amicosante, G., Rossolini, G. M., Galleni, M., Frère, J. M. and Dideberg, O. (2003) The 1.5-Å structure of *Chryseobacterium meningosepticum* zinc β-lactamase in complex with the inhibitor, D-captopril. J. Biol. Chem. **278**, 23868–23873
20 Liénard, B. M. R., Garau, G., Horsfall, L., Karsisiotis, A. I., Damblon, C., Lassaux, P., Papamicael, C., Roberts, G. C. K., Galleni, M., Dideberg, O. et al. (2008) Structural basis for the broad-spectrum inhibition of metallo-β-lactamases by thiols. Org. Biomol. Chem. **6**, 2282–2294
21 Mollard, C., Moali, C., Papamicael, C., Damblon, C., Vessilier, S., Amicosante, G., Schofield, C. J., Galleni, M., Frère, J. M. and Roberts, G. C. K. (2001) Thiomandelic acid, a broad spectrum inhibitor of zinc β-lactamases-kinetic and spectroscopic studies. J. Biol. Chem. **276**, 45015–45023
22 Siemann, S., Evanoff, D. P., Marrone, L., Clarke, A. J., Viswanatha, T. and Dmitrienko, G. I. (2002) N-arylsulfonyl hydrazones as inhibitors of IMP-1 metallo-β-lactamase. Antimicrob. Agents Chemother. **46**, 2450–2457
23 Lassaux, P., Hamel, M., Gulea, M., Delbruck, H., Mercuri, P. S., Horsfall, L., Dehareng, D., Kupper, M., Frère, J. M., Hoffmann, K. et al. (2010) Mercapto phosphonate compounds as broad-spectrum inhibitors of the metallo-β-lactamases. J. Med. Chem. **53**, 4862–4876
24 Siemann, S., Clarke, A. J., Viswanatha, T. and Dmitrienko, G. I. (2003) Thiols as classical and slow-binding inhibitors of IMP-1 and other binuclear metallo-β-lactamases. Biochemistry **42**, 1673–1683
25 Goto, M., Takahashi, T., Yamashita, F., Koreeda, A., Mori, H., Ohta, M. and Arakawa, Y. (1997) Inhibition of the metallo-β-lactamase produced from *Serratia marcescens* by thiol compounds. Biol. Pharm. Bull. **20**, 1136–1140
26 Wachino, J., Yamaguchi, Y., Mori, S., Kurosaki, H., Arakawa, Y. and Shibayama, K. (2013) Structural insights into the subclass B3 metallo-β-lactamase SMB-1 and the mode of inhibition by the common metallo-β-lactamase inhibitor mercaptoacetate. Antimicrob. Agents Chemother. **57**, 101–109
27 Damblon, C., Jensen, M., Ababou, A., Barsukov, I., Papamicael, C., Schofield, C. J., Olsen, L., Bauer, R. and Roberts, G. C. K. (2003) The inhibitor thiomandelic acid binds to both metal ions in metallo-β-lactamase and induces positive cooperativity in metal binding. J. Biol. Chem. **278**, 29240–29251
28 Toney, J. H., Fitzgerald, P. M. D., Grover-Sharma, N., Olson, S. H., May, W. J., Sundelof, J. G., Vanderwall, D. E., Cleary, K. A., Grant, S. K., Wu, J. K. et al. (1998) Antibiotic sensitization using biphenyl tetrazoles as potent inhibitors of *Bacteroides fragilis* metallo-β-lactamase. Chem. Biol. **5**, 185–196
29 Huntley, J. J. A., Fast, W., Benkovic, S. J., Wright, P. E. and Dyson, H. J. (2003) Role of a solvent-exposed tryptophan in the recognition and binding of antibiotic substrates for a metallo-β-lactamase. Protein Sci. **12**, 1368–1375
30 Moali, C., Anne, C., Lamotte-Brasseur, J., Groslambert, S., Devreese, B., Van Beeumen, J., Galleni, M. and Frère, J. M. (2003) Analysis of the importance of the metallo-β-lactamase active site loop in substrate binding and catalysis. Chem. Biol. **10**, 319–329
31 Karsisiotis, A. I., Damblon, C. F. and Roberts, G. C. K. (2013) Complete ^{1}H, ^{15}N and ^{13}C resonance assignments of *Bacillus cereus* metallo-β-lactamase and its complex with the inhibitor *R*-thiomandelic acid. Biomol. NMR Assignments, doi:10.1007/s12104-013-9507-1
32 Marion, D., Kay, L. E., Sparks, S. W., Torchia, D. A. and Bax, A. (1989) 3-Dimensional heteronuclear NMR of N-15-labeled proteins. J. Am. Chem. Soc. **111**, 1515–1517
33 Pascal, S. M., Muhandiram, D. R., Yamazaki, T., Forman-Kay, J. D. and Kay, L. E. (1994) Simultaneous acquisition of N-15-edited and C-13-edited NOE spectra of proteins dissolved in H_2O. J. Magn. Reson., Ser. B **103**, 197–201
34 Zuiderweg, E. R. P., McIntosh, L. P., Dahlquist, F. W. and Fesik, S. W. (1990) 3-Dimensional C-13-resolved proton NOE spectroscopy of uniformly C-13-labeled proteins for the NMR assignment and structure determination of larger molecules. J. Magn. Reson. **86**, 210–216
35 Zwahlen, C., Legault, P., Vincent, S. B. F., Greenblatt, J., Konrat, R. and Kay, L. E. (1997) Methods for measurement of intermolecular NOEs by multinuclear NMR spectroscopy: application to a bacteriophage λ N-Peptide/*boxB* RNA complex. J. Am. Chem. Soc. **119**, 6711–6721
36 Jardetzky, O. and Roberts, G. C. K. (1981) NMR in Molecular Biology. Academic Press, New York
37 Cheung, H. T. A., Searle, M. S., Feeney, J., Birdsall, B., Roberts, G. C. K., Kompis, I. and Hammond, S. J. (1986) Trimethoprim binding to *Lactobacillus casei* dihydrofolate reductase: a C-13 NMR-study using selectively C-13-enriched trimethoprim. Biochemistry **25**, 1925–1931
38 Herrmann, T., Guntert, P. and Wuthrich, K. (2002) Protein NMR structure determination with automated NOE assignment using the new software CANDID and the torsion angle dynamics algorithm DYANA. J. Mol. Biol. **319**, 209–227
39 Guntert, P. (2004) Automated NMR structure calculation with CYANA. Methods Mol. Biol. **278**, 353–378
40 Reference deleted
41 Cornilescu, G., Delaglio, F. and Bax, A. (1999) Protein backbone angle restraints from searching a database for chemical shift and sequence homology. J. Biomol. NMR **13**, 289–302
42 Guntert, P. and Wuthrich, K. (1991) Improved efficiency of protein structure calculations from NMR data using the program DIANA with redundant dihedral angle constraints. J. Biomol. NMR **1**, 447–456

43 Laskowski, R. A., Rullmann, J. A. C., MacArthur, M. W., Kaptein, R. and Thornton, J. M. (1996) AQUA and PROCHECK-NMR: programs for checking the quality of protein structures solved by NMR. J. Biomol. NMR **8**, 477–486

44 Vriend, G. (1990) WHAT IF: a molecular modeling and drug design program. J. Mol. Graphics **8**, 52–56

45 Koradi, R., Billeter, M. and Wuthrich, K. (1996) MOLMOL: a program for display and analysis of macromolecular structures. J. Mol. Graphics **14**, 51–55

46 Carfi, A., Duee, E., Galleni, M., Frère, J. M. and Dideberg, O. (1998) 1.85 Å resolution structure of the zinc(II) β-lactamase from *Bacillus cereus*. Acta Crystallogr., Sect. D: Biol. Crystallogr. **54**, 313–323

47 Fabiane, S. M., Sohi, M. K., Wan, T., Payne, D. J., Bateson, J. H., Mitchell, T. and Sutton, B. J. (1998) Crystal structure of the zinc-dependent β-lactamase from *Bacillus cereus* at 1.9 Å resolution: binuclear active site with features of a mononuclear enzyme. Biochemistry **37**, 12404–12411

48 Scrofani, S. D. B., Chung, J., Huntley, J. J. A., Benkovic, S. J., Wright, P. E. and Dyson, H. J. (1999) NMR characterization of the metallo-β-lactamase from *Bacteroides fragilis* and its interaction with a tight-binding inhibitor: role of an active-site loop. Biochemistry **38**, 14507–14514

49 Kim, Y., Cunningham, M. A., Mire, J., Tesar, C., Sacchettini, J. and Joachimiak, A. (2013) NDM-1, the ultimate promiscuous enzyme: substrate recognition and catalytic mechanism. FASEB J. **27**, 1917–1927

50 Yamaguchi, Y., Jin, W., Matsunaga, K., Ikemizu, S., Yamagata, Y., Wachino, J. I., Shibata, N., Arakawa, Y. and Kurosaki, H. (2007) Crystallographic investigation of the inhibition mode of a VIM-2 metallo-β-lactamase from *Pseudomonas aeruginosa* by a mercaptocarboxylate inhibitor. J. Med. Chem. **50**, 6647–6653

51 Huntley, J. J. A., Scrofani, S. D. B., Osborne, M. J., Wright, P. E. and Dyson, H. J. (2000) Dynamics of the metallo-β-lactamase from *Bacteroides fragilis* in the presence and absence of a tight-binding inhibitor. Biochemistry **39**, 13356–13364

52 Leiros, H.-K. S., Borra, P. S., Bransdal, B. O., Edvardsen, K. S. W., Spencer, J., Walsh, T. R. and Samuelsen, O. (2012) Crystal structure of the mobile metallo-β-lactamase AIM-1 from *Pseudomonas aeruginosa*: insights into antibiotic binding and the role of Gln157. Antimicrob. Agents Chemother. **56**, 4341–4353

53 Greenlee, M. L., Laub, J. B., Balkovec, J. M., Hammond, M. L., Hammond, G. G., Pompliano, D. L. and Epstein-Toney, J. H. (1999) Synthesis and SAR of thioester and thiol inhibitors of IMP-1 metallo-β-lactamase. Bioorg. Med. Chem. Lett. **9**, 2549–2554

54 Garcia-Saez, I., Mercuri, P. S., Papamicael, C., Kahn, R., Frère, J. M., Galleni, M., Rossolini, G. M. and Dideberg, O. (2003) Three-dimensional structure of FEZ-1, a monomeric subclass B3 metallo-β-lactamase from *Fluoribacter gormanii*, in native form and in complex with D-captopril. J. Mol. Biol. **325**, 651–660

55 Heinz, U., Bauer, R., Wommer, S., Meyer-Klaucke, W., Papamichaels, C., Bateson, J. and Adolph, H. W. (2003) Coordination geometries of metal ions in D- or L-captopril-inhibited metallo-β-lactamases. J. Biol. Chem. **278**, 20659–20666

56 Bounaga, S., Galleni, M., Laws, A. P. and Page, M. I. (2001) Cysteinyl peptide inhibitors of *Bacillus cereus* zinc β-lactamase. Bioorg. Med. Chem. **9**, 503–510

57 Sun, Q., Law, A., Crowder, M. W. and Geysen, H. M. (2006) Homo-cysteinyl peptide inhibitors of the L1 metallo-β-lactamase, and SAR as determined by combinatorial library synthesis. Bioorg. Med. Chem. Lett. **16**, 5169–5175

58 Docquier, J. D., Lamotte-Brasseur, J., Galleni, M., Amicosante, G., Frère, J. M. and Rossolini, G. M. (2003) On functional and structural heterogeneity of VIM-type metallo-β-lactamases. J. Antimicrob. Chemother. **51**, 257–266

59 Ullah, J. H., Walsh, T. R., Taylor, I. A., Emery, D. C., Verma, C. S., Gamblin, S. J. and Spencer, J. (1998) The crystal structure of the L1 metallo-β-lactamase from *Stenotrophomonas maltophilia* at 1.7 Å resolution. J. Mol. Biol. **284**, 125–136

60 Nauton, L., Kahn, R., Garau, G., Hernandez, J. F. and Dideberg, O. (2008) Structural insights into the design of inhibitors for the L1 metallo-β-lactamase from *Stenotrophomonas maltophilia*. J. Mol. Biol. **375**, 257–269

Received 30 July 2013/17 September 2013; accepted 24 September 2013
Published as BJ Immediate Publication 24 September 2013, doi:10.1042/BJ20131003

Biochem. J. (2013) **456**, 397–407 (Printed in Great Britain) doi:10.1042/BJ20131003

online data

SUPPLEMENTARY ONLINE DATA

Solution structures of the *Bacillus cereus* metallo-β-lactamase BcII and its complex with the broad spectrum inhibitor *R*-thiomandelic acid

Andreas Ioannis KARSISIOTIS*†, Christian F. DAMBLON*‡ and Gordon C. K. ROBERTS*[1]

*The Henry Wellcome Laboratories of Structural Biology, Department of Biochemistry, University of Leicester, Leicester LE1 9HN, U.K., †The School of Pharmacy and Pharmaceutical Sciences, Biomedical Sciences Research Institute, University of Ulster, Coleraine BT52 1SA, Northern Ireland, U.K., and ‡Chimie Biologique Structurale, Institut de Chimie, Université de Liège, 4000 Liège, Belgium

EXPERIMENTAL

Incorporation of the zinc atoms and the inhibitor molecule into CYANA during structure refinement

The structure determination and automated assignment module used in the present study did not take into account the presence of the two metal atoms or, in the case of the complex, the inhibitor molecule. These were incorporated through the use of the generic linker system present in CYANA. (The NOE-based constraint sets used in refinement were obtained with automated NOE assignment without the use of the linker system.) The residue 'ION' from the standard library was modified to a ZN residue and accordingly the 'METAL' atomtypes entry in the standard library was modified to ZINC. Following the last residue of the protein sequence (Lys^{227}) and the connecting linker residue (PL228), a 12 residue linker was used to connect to the first zinc atom ZN241, comprising ten LL5-type linker residues flanked by LL2-type linker residues. An identical segment was used to connect to the second zinc atom ZN254. The length of the linker segment was chosen to be of sufficient length to ensure minimum steric interference. The effect of the presence of the linker system, with the zinc atoms both fixed and unfixed, on the CYANA target function was examined with an identical set of constraints during refinement. No significant impact was detected by comparison with a refinement run lacking the linker system. The zinc atoms were fixed to the corresponding atoms of the metal-co-ordinating residues with the use of a set of six lower (lol) and upper (upl) distance bounds (for His^{86}, His^{88}, Asp^{90}, His^{149} and Cys^{168}: lol = 2.2, upl = 2.4, and for His^{210}: lol = 2.3, upl = 2.5) loosely based on the distances observed in the di-zinc X-ray structure PDB code 1BVT; in addition, a Zn–Zn interatomic distance was included (lol = 3.65, upl = 3.85) (Table S1).

In similar fashion, the inhibitor molecule was successfully incorporated into the linker system by using a novel residue definition including a cluster of pseudoatoms to ensure correct connectivity with the linker system. The PDB file of the inhibitor was read into MOLMOL [1] and the appropriate dihedral angles were defined (LB1, CHI1, CHI2, CHI3 and LB2). The atom names and types were in accordance with the IUPAC nomenclature and the CYANA 2.1 naming conventions. The dihedral angle and the atom declarations were ordered so as to be compatible with the tree structure of the dihedral angles (SYBYL 7.2 interface to DYANA). Pseudoatoms were added for the thiomandelate aromatic ring protons (QG for HG1 and HG2, QD for HD1 and HD2, and QR for all the ring protons). The creation of the overlap atoms at the beginning and end of the residue definition (corresponding to N, CA and C in the case of amino acids) which ensure the connectivity of the new residue with the generic linker residues was essential since thiomandelate is not an amino acid derivative. A connecting system such as the one used in the creation of proxy residues [2] was used successfully.

Structure calculation and refinement

Simulated annealing

It has been reported, in the case of structural calculations performed with the program ARIA, that an increase in the number of simulated annealing steps can prove to be highly beneficial in achieving convergence, especially large proteins where chemical shift degeneracy is a significant issue [3,4]. In the present study we found that the use of extended torsion angle dynamics (TAD) steps (15 times the normal) can indeed be beneficial in terms of convergence and target function values. However, these calculations tended to become biased towards similar conformations, as reflected by the unusually low RMSD values observed even in some regions expected to be unstructured. This suggests that extended TAD steps can be valuable, providing converged and essentially correct structures and reducing exhaustive peak list analysis, but must be used with caution.

Dihedral angle constraints

We found that too general a use of dihedral angle constraints derived from the TALOS database may introduce erroneous features in regions of unusual or complex backbone structure distribution, for example around the zinc co-ordination sites. Consequently, the structures reported in the present study were calculated both with and without dihedral angle constraints and we focus on the structures obtained without these constraints. Table 1 in the main text gives the structural statistics for the structures calculated without dihedral angle constraints. Table S2 gives these statistics for structures calculated with these constraints. The structures calculated with and without dihedral angle constraints had very similar RMSD values (0.35–0.38 for backbone atoms) and similar Ramachandran statistics (>98 % of residues in the core and allowed regions), but the structures calculated with dihedral angle constraints showed significantly more distance and angle violations.

[1] To whom correspondence should be addressed (email gcr@le.ac.uk).

The complete ^{1}H, ^{13}C and ^{15}N chemical shifts and NMR restraints have been deposited in the BioMagResBank (BMRB) under accession codes 19047 (BcII) and 19048 (BcII–*R*-thiomandelic acid) and co-ordinates have been deposited in the PDB under accession codes 2M5C (BcII) and 2M5D (BcII–*R*-thiomandelic acid).

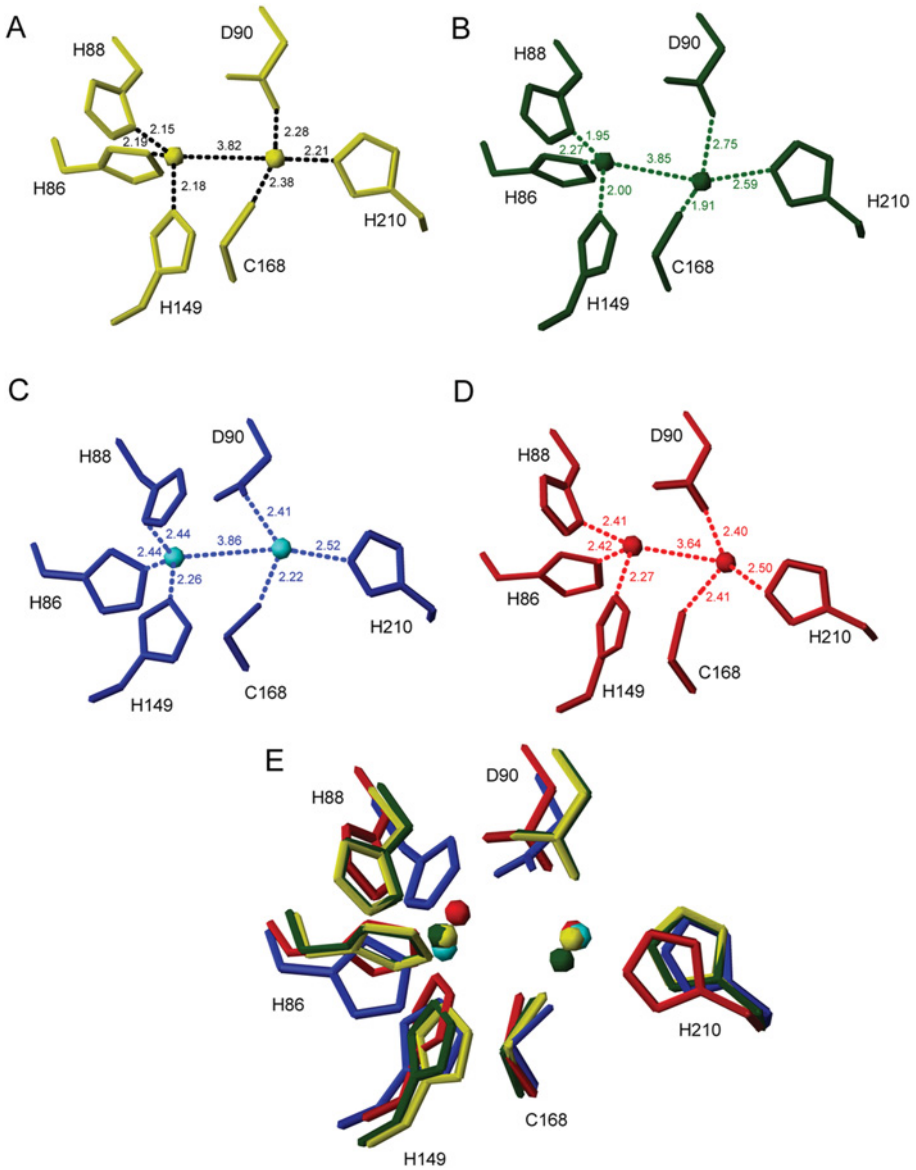

Figure S1 Comparison of zinc co-ordination in solution and in crystal

The co-ordination of the two zinc atoms by protein ligands in BclI in the free enzyme in crystal (**A**, PDB code 1BVT; **B**, PDB code 1BC2) and in solution (**C**) and in the BclI–thiomandelate complex in solution (**D**) are shown separately (**A**–**D**) and superimposed (**E**).

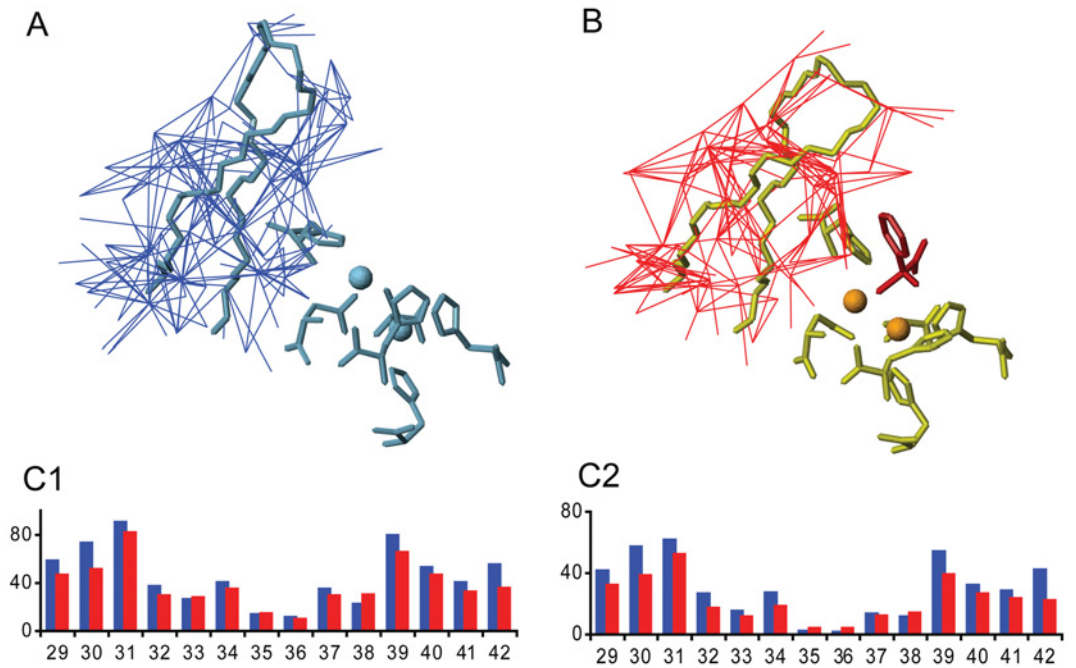

Figure S2 Constraints defining the conformation of the β3–β4 loop

The NOE constraints, including both those involving side chain atoms and those involving backbone atoms, are shown on backbone representations of the loop (residues 29–42) for (**A**) the free enzyme and (**B**) the *R*-thiomandelate complex. The two panels share the same orientation and the inhibitor molecule is presented in red. (**C**) Constraint distribution for residues 29–42, showing total number of constraints (**C1**) and long plus medium range constraints (**C2**); free enzyme constraints are shown in blue, complex constraints in red.

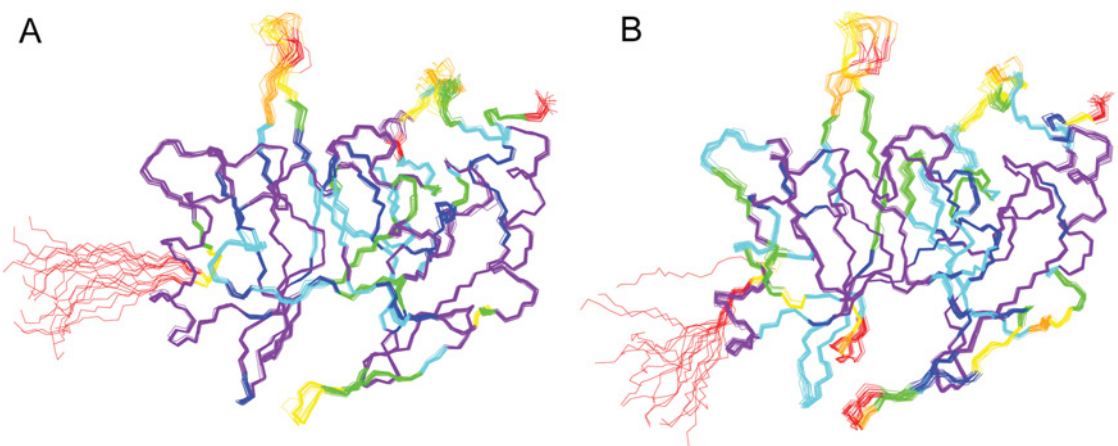

Figure S3 Local backbone RMSDs

Local backbone RMSDs are shown on the solution structures of the free enzyme (**A**) and the complex (**B**) in rainbow colours: violet ($\leqslant$0.03 Å), blue (0.03–0.04 Å), cyan (0.05–0.06 Å), green (0.07–0.09 Å), yellow (0.1–0.2 Å), orange (0.2–0.3 Å) and red ($>$0.3 Å).

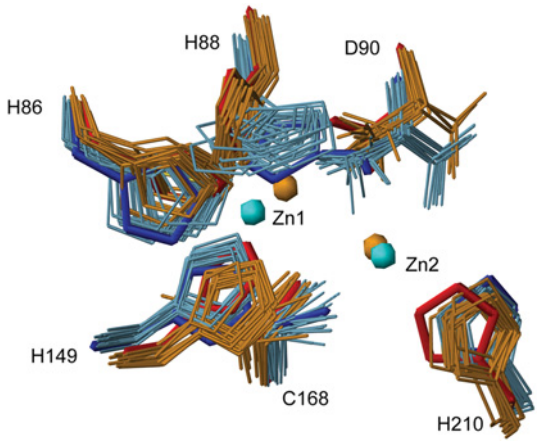

Figure S4 Zinc atoms and their protein ligands in the structures of the free enzyme and the *R*-thiomandelate complex

The bundles of structures shown were determined solely from the NOE-based constraints, before the introduction of zinc restraints in refinement. Structures are shown for the free enzyme (slate blue) and the complex (orange). The positions of the protein ligands after refinement are shown in blue (free enzyme) and red (complex) and the positions of the zinc atoms as blue (free enzyme) and orange (complex) spheres.

Table S1 Metal co-ordination constraints used (lower and upper limits) and corresponding distances on the X-ray structure (PDB code 1BVT) and both NMR structures

Bundles of 20 NMR structures were used for the distance calculations. RTM, *R*-thiomandelate.

Distance	lol	upl	1BVT	BclI	BclI–RTM
His^{86} NE2–Zn1	2.20	2.40	2.33	2.40–2.46	2.42–2.47
His^{88} ND1–Zn1	2.20	2.40	2.24	2.40–2.48	2.18–2.43
His^{149} NE2–Zn1	2.20	2.40	2.32	2.16–2.40	2.27–2.42
Cys^{168} SG–Zn2	2.20	2.40	2.29	2.19–2.41	2.24–2.44
His^{210} NE2–Zn2	2.30	2.50	2.41	2.50–2.53	2.29–2.51
Asp^{90} OD2–Zn2	2.20	2.40	2.29	2.23–2.43	2.19–2.43
Zn1–Zn2	3.65	3.85	3.75	3.82–3.88	3.62–3.65

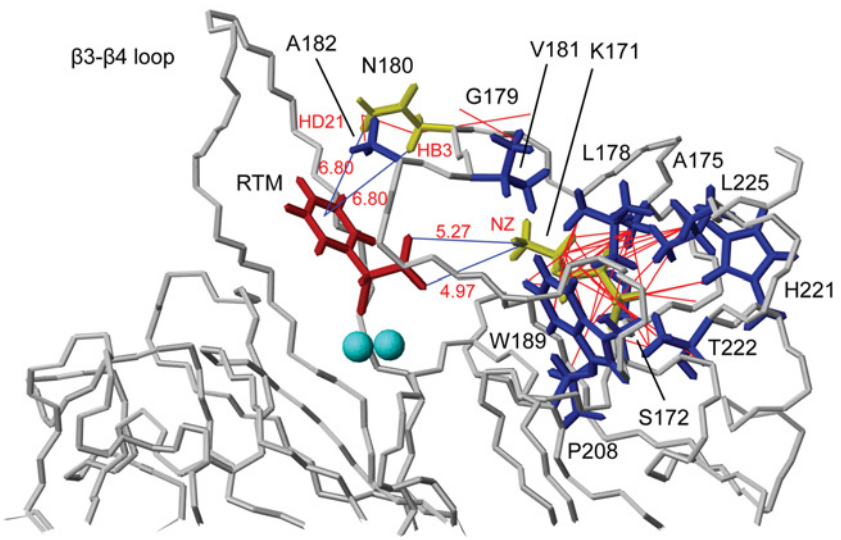

Figure S5 Conformations of Lys^{171} and Asn^{180} in the BclI–thiomandelate complex

The side chains of Lys^{171} and Asn^{180} are shown in yellow and thiomandelate in red. The constraint network defining the positions of Lys^{171} and Asn^{180} is depicted with red lines and the side chains of the residues involved in these constraints are shown in blue. The distances between the NZ atom of Lys^{171} and the oxygen atoms of the carboxylate group of the inhibitor and the distances between the HD21 and HB3 atoms of the Asn^{180} and the QR pseudo atom of the aromatic ring of the inhibitor are indicated. The zinc atoms are shown as cyan spheres and the protein backbone is coloured grey.

Table S2 Structural statistics and agreement with experimental data for the refined BcII and BcII–*R*-thiomandelate structures calculated with external (TALOS) dihedral angle input

Target function, RMSD and energy are calculated for a bundle of 20 structures unless specified otherwise. RTM, *R*-thiomandelate.

Parameter	Statistics	BcII	BcII–*R*-thiomandelate
CYANA/CANDID	Input peaks	13088	12499
	Unassigned peaks	1082	1159
	Assignment percentage	91.7	90.7
	Target function (cycle1)	233.87	195.59
	Target function (final)	5.39	3.81
RMSD, Å (residues 7–227) cycle1	Backbone/heavy atoms	0.85/1.30	0.95/1.39
RMSD, Å (residues 7–227) final	Backbone/heavy atoms	0.30/0.66	0.31/0.67
NOE constraints	Upper distance limits	7165	6565
	Short range ($i = 1$)	3004	2815
	Medium range ($1<i\leqslant4$)	1257	1098
	Long range ($i>4$)	2904	2652
	Removed during refinement	104	2
Other constraints	Non-NOE constraints (zinc)	7	9
	RTM constraints	–	13
	Dihedral restraints	206	202
	Hydrogen bonds	0	50
	Stereospecific assignments	142	111
Target function (refinement)	Minimum	2.52	2.97
	Average (20 structures)	3.1$\pm$0.3	3.3$\pm$0.2
	Average (50 structures)	4.3$\pm$1.6	3.5$\pm$0.2
RMSDs of experimental restraints (20 structures)	Upls	0.006$\pm$0.001	0.006$\pm$0.0003
	Lols	0.002$\pm$0.002	0.005$\pm$0.001
	Torsion angles	0.23$\pm$0.06	0.21$\pm$0.03
Van der Waals energy sums	20 structures	14.3$\pm$0.7	14.1$\pm$0.7
	50 structures	16.19$\pm$2.34	14.88$\pm$0.82
Mean violations (20/50 structures)	Distance >0.5 Å	0.3$\pm$0.4/0.6$\pm$0.7	0/0
	Angle >5°	0.05$\pm$0.22/1.0$\pm$2.8	0/0
	Van der Waals	0/0	0/0
RMSD (residues 7–227) final structures	Backbone/heavy atoms	0.38/0.72	0.38/0.72
Ramachandran statistics (CANDID stage/refinement)	Core (%)	78.6/78.7	78.2/76.6
	Allowed (%)	20.9/20.0	21.3/22.0
	Generously allowed (%)	0.1/0.6	0.1/0.8
	Disallowed (%)	0.5/0.6	0.5/0.6

REFERENCES

1 Koradi, R., Billeter, M. and Wuthrich, K. (1996) MOLMOL: a program for display and analysis of macromolecular structures. J. Mol. Graphics **14**, 51–55

2 Ab, E., Pugh, D. J. R., Kaptein, R., Boelens, R. and Bonvin, A. (2006) Direct use of unassigned resonances in NMR structure calculations with proxy residues. J. Am. Chem. Soc. **128**, 7566–7571

3 Fossi, M., Linge, J., Labudde, D., Leitner, D., Nilges, M. and Oschkinat, H. (2005) Influence of chemical shift tolerances on NMR structure calculations using ARIA protocols for assigning NOE data. J. Biomol. NMR **31**, 21–34

4 Fossi, M., Oschkinat, H., Nilges, M. and Ball, L. J. (2005) Quantitative study of the effects of chemical shift tolerances and rates of SA cooling on structure calculation from automatically assigned NOE data. J. Magn. Reson. **175**, 92–102

Received 30 July 2013/17 September 2013; accepted 24 September 2013
Published as BJ Immediate Publication 24 September 2013, doi:10.1042/BJ20131003